ISSN 1392-1207. MECHANIKA. Vol. 32, No. 3, 2026: 177–184

CFD-Predicted Rotordynamic Characteristics for Labyrinth Seal Under Gas-Liquid Two-Phase Conditions

Bo ZHANG*, Qiang MA,***, Pingwei CHEN****, Qingfeng DUAN**,***, Wensheng MA*, Sichen LI**,***, Guangbin YU*****

*Chongqing Pump Industry, Chongqing 400033, China

**Beijing Research Center, CNOOC Research Institute Co., Ltd., Beijing 100028, China

***National Energy Deepwater Oil and Gas Engineering Technology Research and Development Center, Beijing 100028, China

****Chongqing Research Institute, Harbin Institute of Technology, Chongqing 401120, China,
E-mail: 297183138@qq.com (Corresponding Author)

*****Harbin Institute of Technology, Harbin 150000, China

https://doi.org/10.5755/j02.mech.44178

Nomenclature

K - Direct stiffness, N/m; k - Cross coupling stiffness, N/m; m - Cross coupling virtual-mass, kg; M - Direct virtual-mass, kg; C - Direct damping, Ns/m; c - Cross coupling damping, Ns/m; K_{eff} - Effective stiffness, N/m; C_{eff} - Effective damping, Ns/m; Fr - Response force in radial direction, N; Ft - Response force in tangential direction, N; n - Rotor speed, r/min.

1. Introduction

As a core fluid machinery widely used in strategic industries such as nuclear energy, petrochemical engineering, and marine engineering, gas-liquid two-phase pumps undertake the critical task of transporting multiphase media with complex components and variable physical properties [1-3]. Especially in the fourth-generation sodium-cooled fast reactor (SFR) system, the primary and secondary circuit sodium pumps, as the "power core" of the coolant circulation system, are prone to gas entrainment in the working medium during actual operation, forming a gas-liquid two-phase flow state [4,5]. As a key component of gas-liquid two-phase pumps, labyrinth seals directly dominate leakage control, energy efficiency, and rotordynamic stability under extreme conditions of high temperature, high speed, and high pressure. Their performance reliability is not only related to the safe and efficient operation of the pump itself but also becomes a core technical bottleneck restricting the industrialization of advanced energy equipment such as sodium-cooled fast reactors [6,7].

The unique thermophysical properties of gas-liquid two-phase media, combined with the complex flow behavior in the seal clearance, make the rotordynamic characteristics of labyrinth seals more complex than those under single-phase conditions. Unlike traditional single-phase liquid seals (e.g., pure water and lubricating oil seals), the interaction between gas and liquid phases in the seal clearance leads to nonlinear changes in flow field distribution, pressure pulsation, and viscous shear effect [8-10]. At present, existing research in the field of gas-liquid two-phase pumps mainly focuses on hydraulic performance optimization and cavitation characteristics, while systematic studies on the rotordynamic behavior of labyrinth seals under the coupling effect of pressure drop, rotor speed, and gas volume fraction (GVF) are still scarce [2,11]. This research gap severely restricts the accurate prediction and optimal design of gas-liquid two-phase pump seal systems.

In the field of seal rotordynamic characteristic analysis, numerical simulation has gradually replaced experimental methods as the mainstream technical means due to its strong controllability and high cost-effectiveness [2]. The bulk-flow model was once widely used to calculate the rotordynamic coefficients of liquid annular seals, but its calculation accuracy in complex gas-liquid two-phase systems and extreme operating conditions is insufficient due to the limitations of simplified assumptions about flow field distribution [12]. With the development of computational fluid dynamics (CFD) technology, the transient CFD method based on dynamic mesh technology and multi-frequency rotor whirling model has become a cutting-edge tool for high-precision simulation [13-15]. This method can accurately capture the transient flow field evolution caused by rotor whirling and rotation, reliably extract frequency-dependent rotordynamic coefficients, and provide an ideal technical route for solving the rotordynamic analysis of gas-liquid two-phase labyrinth seals. However, the application of this method in labyrinth seals of gas-liquid two-phase pumps still needs further improvement.

To fill the aforementioned research gaps and lay a theoretical foundation for the optimal design of the sealing system of gas-liquid two-phase pumps, this study takes the water-air gas-liquid two-phase mixture as the research object and adopts a transient CFD method to systematically investigate the rotordynamic characteristics of labyrinth seals. The rotational and whirling motions of the rotor are realized via the macro commands of user-defined functions (UDFs), namely DEFINE_CG_MOTION and DEFINE_PROFILE; the whirling equation of the rotor is derived in detail, and the eccentric motion of the rotor is simulated by combining the dynamic mesh technique.

This study clarifies the inherent variation laws of the rotordynamic coefficients of gas-liquid two-phase labyrinth seals under the coupling conditions of multiple parameters, reveals the influence mechanism of gas volume fraction on seal stability, and provides key technical support for the design optimization, safety assessment and long-term reliable operation of gas-liquid two-phase pumps in strategic industries such as advanced nuclear energy.

2. Computational Theory

The medium investigated in this paper is a gas-liquid fluid mixture. The continuity equation for the mixture is:

$$\frac{\partial}{\partial t}\rho_m + \nabla\cdot\left(\rho_m v_m\right) = 0\,. \tag{1}$$

The momentum equation of the mixture can be derived from the momentum equations of each phase in the mixed phase:

$$\begin{aligned}&\frac{\partial}{\partial t}\left(\rho_m v_m\right) + \nabla\cdot\left(\rho_m v_m v_m\right) = \\ &= -\nabla p + \nabla\cdot\left[u_m\left(\nabla v_m + \nabla v_m{}^T\right)\right] + \\ &+ \rho_m g_m + F + \nabla\cdot\left(\sum_{k=1}^{n}\alpha_k\rho_k v_{dr,k} v_{dr,k}\right),\end{aligned} \tag{2}$$

where ρ_m is the mixture density, kg/m^3; v_m is the mass-averaged velocity, m/s; u_m is the mixture viscosity coefficient, Pa·s; F is the body force, N; n is the number of phases; α_k is the volume fraction of the k phase; ρ_k is the density of the k phase, kg/m^3; $v_{dr,k}$ is the drift velocity of the k phase, m/s.

The volume fraction equation of the secondary phase p can be derived from the continuity equation of the secondary phase p:

$$\frac{\partial}{\partial t}\left(\rho_p\alpha_p\right) + \nabla\cdot\left(\rho_p\alpha_p v_m\right) = -\nabla\cdot\left(\rho_p\alpha_p v_{dr,p}\right). \tag{3}$$

We assume that the rotor is whirling around its centered position, the tangential force and the radial force can be written [15]:

$$-F_t / e = -k + \Omega^2 m + \Omega C\,, \tag{4}$$

$$-F_r / e = K - \Omega^2 M + \Omega c\,. \tag{5}$$

The effective stiffness and effective damping are often needed to analyze the overall stability characteristics. They are expressed:

$$K_{eff} = -F_r / e\,, \tag{6}$$

$$C_{eff} = \left(-F_t / e\right)/\Omega\,. \tag{7}$$

In the CFD software, the DEFINE_CG_MOTION macro in the User-Defined Function (UDF) is used to realize the whirling motion of the rotor, namely the velocity perturbation and displacement perturbation of the rotor. The velocity equation for its whirling motion can be expressed as:

$$\begin{cases}\dot{x}(t) = -a\Omega_i\sum_{i=1}^{N} sin\left(\Omega_i t\right)\\ \dot{y}(t) = b\Omega_i\sum_{i=1}^{N} cos\left(\Omega_i t\right)\end{cases}. \tag{8}$$

The moving coordinate system is established via the DEFINE_PROFILE control macro, where the actual motion is converted into physical quantities that are embedded into the program for iterative calculation. In this way, the dynamic boundary of rotor rotation is transformed into a static boundary, enabling rotation at an arbitrary position. The rotational motion of the rotor is illustrated in Fig. 1, where the central coordinate represents the absolute coordinate system. In the user-defined functions of Fluent, face zones are obtained by the Thread data type; for the rotating rotor walls at different positions, the begin_f_loop(f,t) macro is adopted to perform face looping, which allows the coordinates of the rotor mesh centers to be acquired. Fig. 1 below shows the positions of the rotating rotor in the four quadrants of the absolute coordinate system, with the coordinate system marked by dashed lines denoting the local coordinate system.

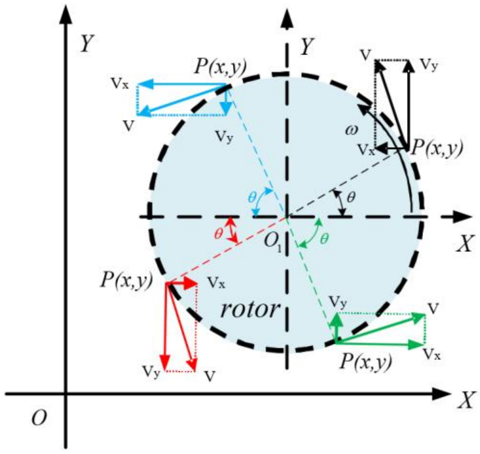

Fig. 1 The coordinate of rotor rotation motion

Assume that there is an arbitrary point $P(x, y)$ on the rotor surface, and its distance from the origin of the rotor coordinate system is equal to the rotor radius:

$$r = \sqrt{\left(x - x_0\right)^2 + \left(y - y_0\right)^2}\,. \tag{9}$$

It can see from Fig. 1 that by synthesizing the velocity components in the first to fourth quadrants, it can be obtained that: when $x < 0$, then $v_y = -v_y$; when $x > 0$, then $v_y = v_y$; when $y < 0$, then $v_x = v_x$; when $y > 0$, then $v_x = -v_x$. The rotor position is accurately determined by writing a UDF program that encodes the rotor's velocity components for any quadrant.

When the rotor rotates from the concentric position to the seal clearance position with an eccentricity of 90% as shown in Fig. 2, a, and as illustrated in Fig. 2, b, the skewness of the maximum mesh increases from 0.035 to 0.26. The increase in mesh skewness indicates a rise in the mesh distortion rate during the rotor's rotation with large eccentricity. Nevertheless, the mesh elements in the clearance still do not exhibit high distortion or negative volumes at this time, which demonstrates that the dynamic mesh algorithm is applicable to the transient flow simulation of the seal.

In numerical calculation, the rotational and whirling motions of the rotor were realized by the UDF program using the transient dynamic mesh analysis technique, and the equations for the orbital and rotating motions of the rotor were established based on the DEFINE_CG_MOTION and DEFINE_PROFILE control macros, respectively. Finally,

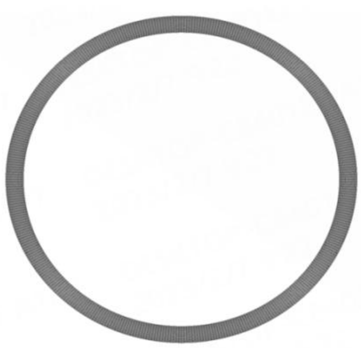

a

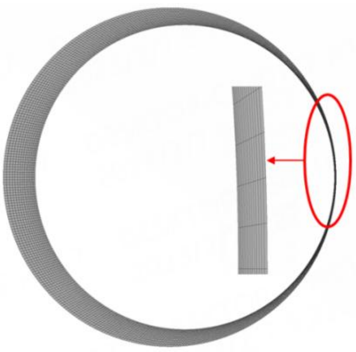

b

Fig. 2 The mesh under the eccentric motion: a – initial mesh, b – deformed mesh

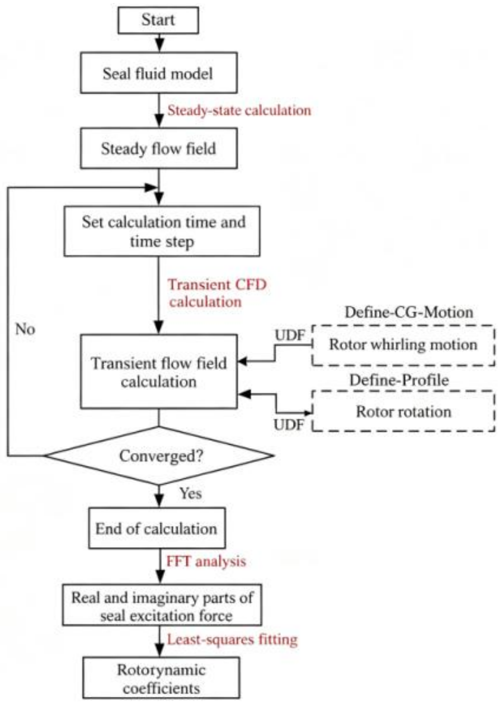

Fig. 3 Calculation flowchart

the numerically calculated seal excitation forces were subjected to FFT transformation to derive their real and imaginary parts, and the dynamic coefficients were obtained via the least square method fitting. The calculation flowchart is shown in Fig. 3.

3. Calculation Model

This paper mainly conducts a study on the mixed fluid of water and air media. Fig. 4 shows the schematic diagram of the grooved seal structure with parallel grooves on the rotor, and its geometric parameters and operating conditions are detailed in Table 1. In this study, analyses were carried out under three different pressure drops, three different rotor rotational speeds and three different gas volume fractions, respectively. Fig. 5 presents the 3D model and mesh generation result of the seal in the Fluent software; all

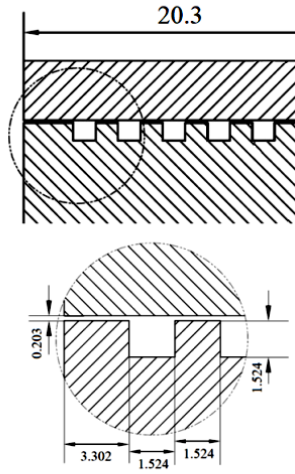

Fig. 4 Geometry of parallel grooved seal

Table 1

Geometry parameters & operational conditions

Inlet Pressure, MPa	0.51, 0.81, 1.11
Outlet Pressure, MPa	0.1
Gas volume fraction, GVF	10%, 20%, 30%
Inlet preswirl ratio λ	0
Rotor speed n, rpm	1500, 3000, 4500
Rotor diameter D, mm	102
Seal radial clearance c_r, mm	0.203
Groove depth d, mm	1.524
Land width w, mm	1.524
Groove length s, mm	1.524

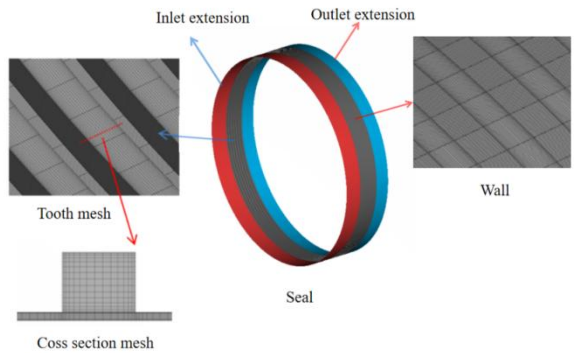

Fig. 5 Computational model and mesh

Table 2

CFD method

Fluids	Mixture (Air/ water)
Inlet boundary condition	Total pressure
Multi-phase	Mixture
Outlet boundary condition	Static pressure
Solution type	Transient
Mesh motion	Dynamic mesh method
Turbulence model	Scalable wall function, k-ε model
Wall property	Adiabatic

mesh elements adopt hexahedrons, and the mesh independence study has been completed. The final mesh scale of the CFD model adopted in this paper is 2.16 million elements.

The *k-ε* turbulence models are more suitable in CFD software. Table 2 gives the transient CFD solution setups.

4. Results and Discussion

4.1. Experiment results

To verify the authenticity of the Computational Fluid Dynamics (CFD) calculation results, a seal test rig with a mixed medium of normal temperature water and air was adopted for the experiment, and the test rig is shown in Fig. 6. The test rig operates at pressure drops up to 1.5 MPa and rotor speeds up to 6000 r/min. Coriolis Mass Flowmeter (accuracy: ±0.5%) is used for leakage flow rate measurement. Pressure transducers (accuracy: ±0.1%, range: 0-2 MPa) are installed at the seal inlet and outlet. Rotor speed is monitored by a tachometer (accuracy: ±0.1%).

Figs. 7 and 8 present the comparisons between the experimental and numerical results of leakage flow rate with respect to pressure difference and rotational speed respectively. It can be seen from the figures that the experimental and numerical results of leakage flow rate exhibit a basically consistent variation trend: the leakage flow rate decreases with the increase in rotational speed and increases with the rise in pressure difference, the maximum relative error between the experimental and numerical results is approximately 22.3%, which is considered acceptable.

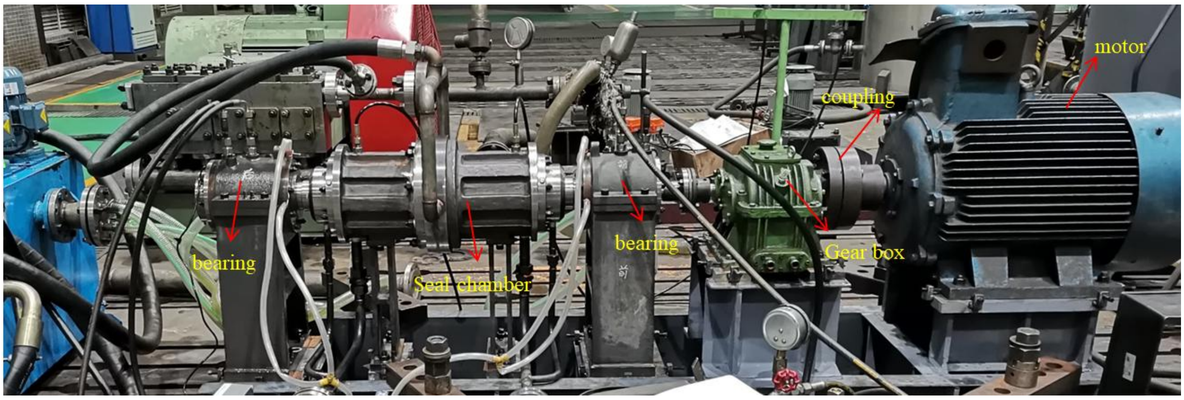

Fig. 6 Test rig

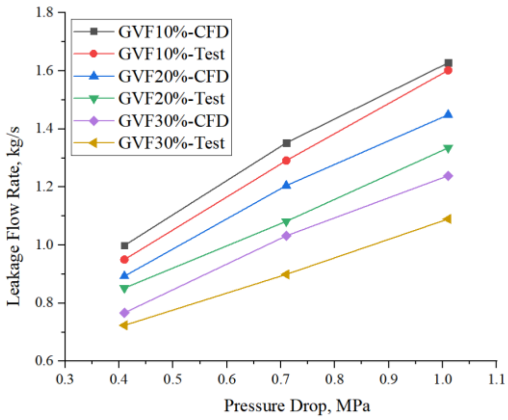

Fig. 7 Calculations versus measured leakage flow rate (n = 3000 r/min)

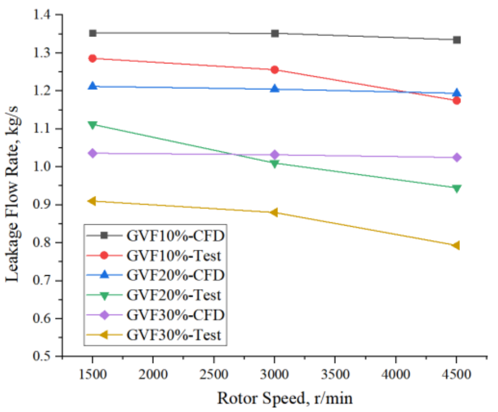

Fig. 8 Calculations versus measured leakage flow rate (Δp = 0.71 MPa)

4.2. Effects of pressure drop

The CFD method was used to analyze the influence of pressure drops on rotordynamic coefficients, it was carried out at three different pressure drops of 0.41 MPa, 0.71 MPa and 1.01 MPa. Fig. 9 presents the variation curves of stiffness and damping coefficients with pressure drop under three gas volume fractions at a rotor speed of 3000 r/min. It can be seen from the figure that the direct stiffness coefficient K increases with the rise of pressure drop for all three gas volume fractions, and the K values show little difference among the three gas volume fractions, with the K decreasing slightly as the gas volume fraction increases. The direct damping coefficient C is positive in all cases; it decreases with the increase of gas volume fraction and increases with the rise of pressure drop. At a pressure drop of 0.71 MPa, the direct damping coefficients C decreases by 22.2% when the gas volume fraction increases from 10% to 30%. The cross-coupling stiffness coefficient k increases with the rise of pressure drop and decreases with the increase of gas volume fraction. The cross-coupling damping coefficient c is negative in all cases, and its absolute value becomes larger with the increase of pressure drop. It can also be observed from the figure that the absolute value of the negative cross-coupling damping coefficient increases as the gas volume fraction rises.

It can be seen from Fig. 10 that the K_{eff} values under the three gas volume fractions are all positive and exhibit a parabolic rising trend; the effective stiffness K_{eff} increases substantially with the increase of pressure drop. Meanwhile, it can be found that the effect of gas volume fraction on effective stiffness K_{eff} is not significant, and the

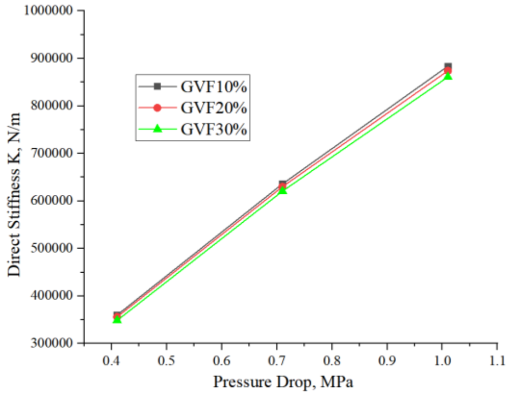

a

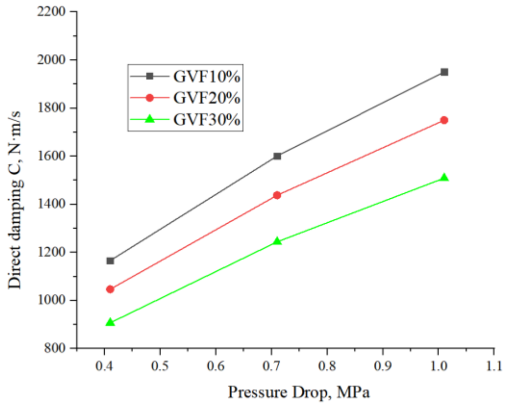

b

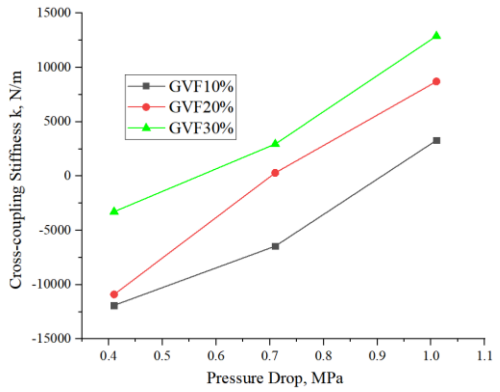

c

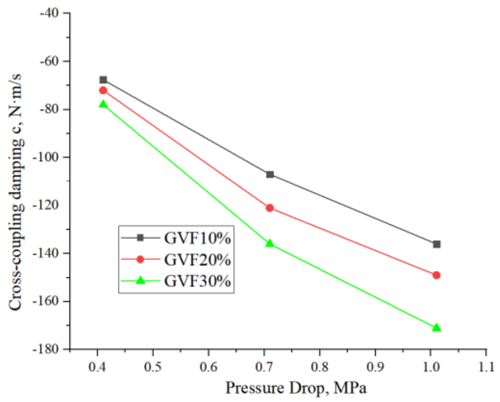

d

Fig. 9 Frequency-independent rotordynamic coefficients versus pressure drop (n = 3000 r/min): a – direct stiffness K, b – direct damping C, c – cross-coupling stiffness k, d – cross-coupling damping c

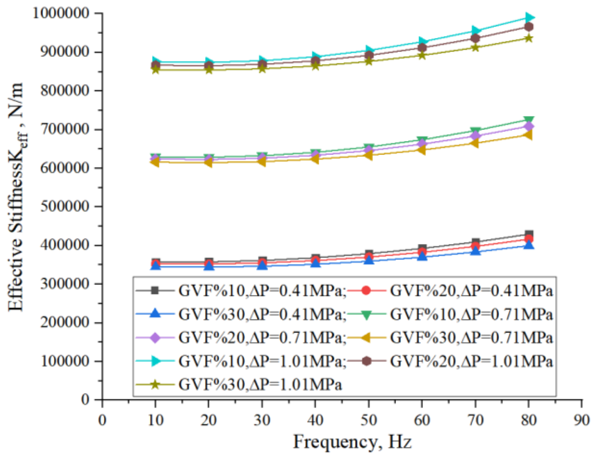

Fig. 10 Frequency-dependent plots of effective stiffness at different pressure drop (n = 3000 r/min)

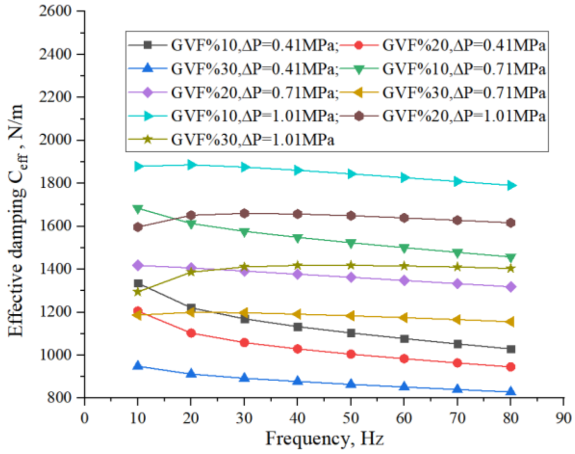

Fig. 11 Frequency-dependent plots of effective damping at different pressure drop (n=3000 r/min)

K_{eff} decreases slightly as the gas volume fraction increases, which is the result of the combined effect of K, M and c.

Fig. 11 shows the variation curves of the frequency-dependent effective damping coefficient C_{eff}, which is jointly affected by C, k and m. The C_{eff} values under the three gas volume fractions are positive over the entire whirling frequency range, and their values increase significantly with the rise of pressure drop; the effective damping coefficient C_{eff} basically shows a decreasing trend with the increase of whirling frequency. At a pressure drop of 1.01 MPa, in the low-frequency range (<20 Hz), the C_{eff} decreases slightly with the increase of whirling frequency. With the increase of gas volume fraction, the effective damping decreases significantly.

4.3. Influence of rotor speed

To analyze the influence of rotor rotational speed on rotor dynamic characteristics, CFD numerical simulations were conducted at rotor speeds of 1500 r/min, 3000 r/min and 4500 r/min for three different gas volume fractions (GVFs), respectively. Fig. 12 presents the variation curves of frequency-independent rotor dynamic coefficients under the working condition of a pressure drop of 0.71 MPa for the three GVFs.

The direct stiffness coefficient K under all three GVFs was positive and increased with the rise of rotor speed,

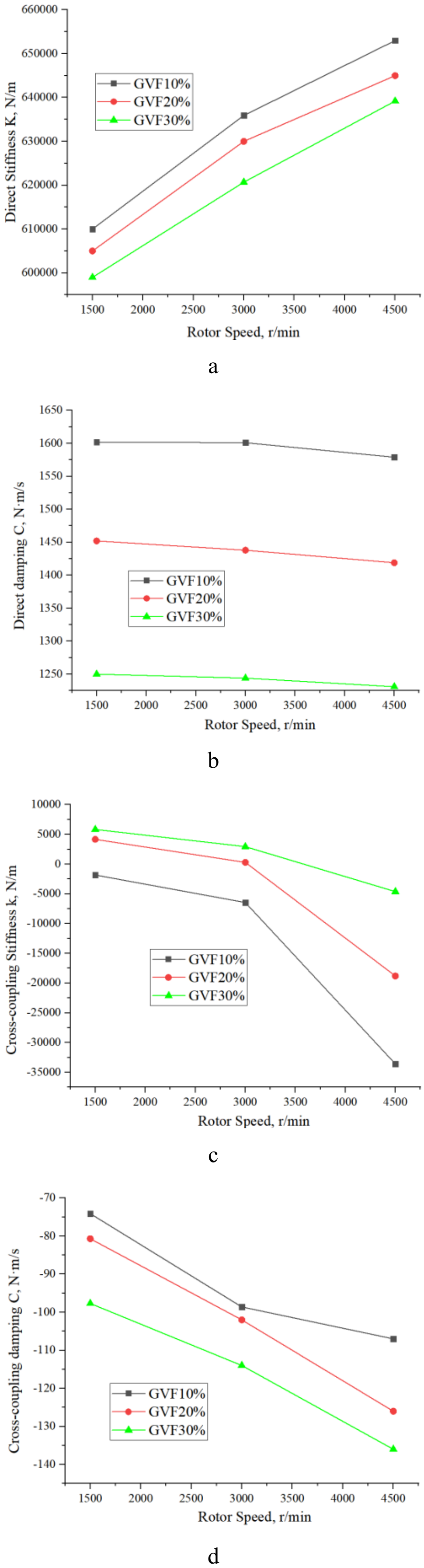

Fig. 12 Frequency-independent rotordynamic coefficients versus rotor speed (Δp = 0.71MPa): a – direct stiffness K, b – direct damping C, c – cross-coupling stiffness k, d – cross-coupling damping c

while the K decreased with the increase of GVF. When the GVF increased from 10% to 30%, the direct stiffness coefficient K experienced a maximum reduction of 2.4%. The direct damping coefficient C under the three GVFs all decreased as the rotor speed rose: as the rotor speed increased from 1500 r/min to 4500 r/min, the direct damping coefficient of GVF 10% decreased by 1.4%, and that of GVF 30% by 1.5%. A lower GVF corresponded to a larger direct damping coefficient. The cross-coupling stiffness k also decreased with the increase of rotor rotational speed. At a rotational speed of 4500 r/min, the cross-coupling stiffness values for all three GVFs were negative, and a lower GVF led to a larger absolute value of the negative stiffness. The cross-coupling damping coefficient c under the three GVFs were all negative and decreased with the rise of rotor speed: as the rotor speed increased from 1500 r/min to 4500 r/min, the cross-coupling damping coefficient c decreased from -74.1 N.m/s to -107.8 N.m/s for GVF 10%, from -80.7 N.m/s to -126.3N.m/s for GVF 20%, and from -97.7 N.m/s to -136.2 N.m/s for GVF 30%.

Fig. 13 shows the variation curves of the frequency-dependent effective stiffness coefficient K_{eff} with whirling frequency. For the three gas volume fractions (GVFs), the K_{eff} exhibits a parabolic variation trend with the whirling frequency, and the effect of rotor speed is significant over the entire frequency range. The parabolic

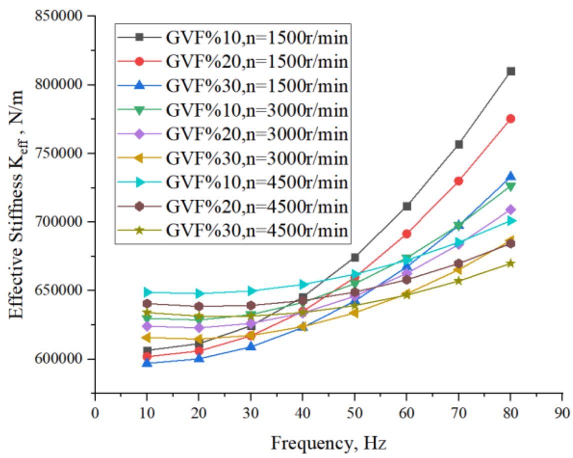

Fig. 13 Frequency-dependent plots of effective stiffness at different rotor speed (Δp = 0.71 MPa)

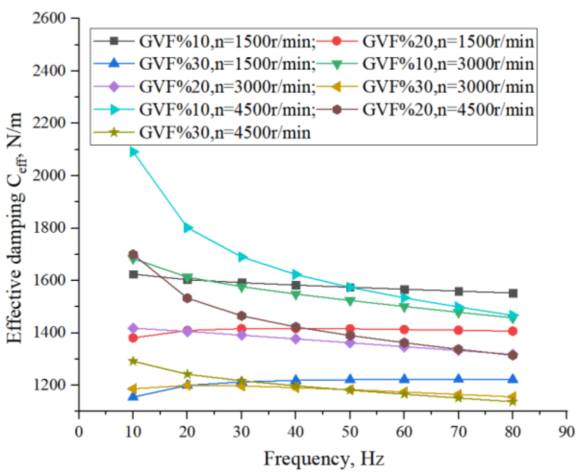

Fig. 14 Frequency-dependent plots of effective damping at different rotor speed (Δp = 0.71 MPa)

curvature is larger at lower rotational speeds, indicating that the effective stiffness coefficient K_{eff} changes more drastically with the variation of whirling frequency under low-speed conditions. The higher the whirling frequency, the larger the K_{eff} value at low rotor speeds. At a fixed rotor speed, the K_{eff} decreases with the increase in GVF, regardless of whether the whirling frequency is high or low. Therefore, under the same operating conditions, a lower GVF results in a superior stiffness performance of K_{eff}.

Fig. 14 presents the variation curves of the frequency-dependent effective damping coefficient C_{eff} with whirling frequency. The C_{eff} is positive over the entire whirling frequency range for all three GVFs. At a rotor speed of 1500 r/min, the variation of C_{eff} is negligible across the entire frequency range, whereas at 4500 r/min, it decreases significantly with the increase in whirling frequency. When the whirling frequency exceeds 50 Hz, the effective damping coefficient C_{eff} at 1500 r/min is higher than that under the other two rotor speed conditions. With the increase in GVF, the C_{eff} decreases significantly under all three rotor speed conditions.

4.4. Discussion

The increase in direct stiffness K with rising pressure drop stems from the Lomakin effect. A larger axial pressure gradient generates stronger hydrodynamic pressure within the seal clearance. Meanwhile, higher axial flow velocity intensifies turbulent dissipation inside the seal cavities, which further raises the direct damping C. The reduction of direct damping C with increasing gas volume fraction (GVF) is fundamentally caused by the weakened squeeze-film effect. Rising GVF reduces the effective bulk modulus of the two-phase mixture. During rotor whirling, the reaction force provided by the liquid film decreases accordingly. Elevated rotor speed intensifies circumferential swirl in the seal clearance, leading to a lower cross-coupling stiffness k and aggravated destabilizing effects of negative cross-coupling damping c.

Design recommendations are summarized from the perspective of optimization: First, for high-GVF operating conditions, reducing the radial seal clearance or smooth annular seals is advised to strengthen the Lomakin effect, simultaneously increasing direct stiffness K and direct damping C to offset performance degradation induced by higher GVF. Second, under high-speed operating conditions where cross-coupling stiffness turns negative, inlet anti-swirl devices can be installed to suppress the inlet fluid preswirl intensity.

5. Conclusions

The transient dynamic mesh method is adopted to calculate the rotordynamic coefficients of the seal under gas-liquid two-phase flow conditions. The leakage flow rate of the seal in two-phase condition is measured experimentally, and the test data show good agreement with the numerical predictions.

We found that pressure drop, rotor speed, and gas volume fraction (GVF) significantly affect rotordynamic coefficients. Higher pressure drop increases K, C, and k, whereas higher GVF reduces all three – C decreases by 22.2% as GVF rises from 10% to 30% at Δp = 0.71 MPa. Higher rotor speed increases K but reduces C; k becomes negative at 4500 r/min; cross-coupling damping c drops from -74.1 to -107.8 N·s/m (GVF 10%) and from -97.7 to -136.2 N·s/m (GVF 30%). The effective damping C_{eff} remains positive across the investigated frequency range, this is beneficial to the stability of the rotor system.

In terms of structural optimization design, for high-GVF operating conditions, it is recommended to reasonably reduce the radial seal clearance to strengthen the Lomakin effect, or adopt smooth annular seal configurations to mitigate internal fluid kinetic energy dissipation. When the rotor operates at high speeds and the cross-coupling stiffness k turns negative, anti-swirl measures shall be implemented to suppress circumferential swirl.

Acknowledgments

This work is supported by National Science and Technology Major Project (Project No.: 2025ZD1403500 and Project No.: 2025ZD1403504), YY Talent Program Project of Chongqing (Project No.: RC-YY-2025-001) and Project of New Chongqing Talent Introduction Program (No.: CSTB2025YCJH-KYXM0004).

References

1. **Zhang, M.; Childs, D. W.** 2021. Experimental Study on the Performance of a See-Through Labyrinth Seal With Two-Phase, Mainly-Liquid Mixtures, ASME Journal of Engineering for Gas Turbines and Power 143(1): 011015. https://doi.org/10.1115/1.4048799.
2. **Osipov, É. V.; Telyakov, É. S.; Latyipov, R. M.; Bugembe, D.** 2019. Influence of Heat and Mass Exchange in a Liquid Ring Vacuum Pump on Its Working Characteristics, Journal of Engineering Physics and Thermophysics 92(4): 1055-1063. https://doi.org/10.1007/s10891-019-02020-7.
3. **Yan, Q.; Li, L.; Tan, Y. F.** 2026. Energy Transfer Characteristics of Surface Vortex Heat Flow Under Non-Isothermal Conditions Based on the Lattice Boltzmann Method, Processes 14(2): 378. https://doi.org/10.3390/pr14020378.
4. **Wang, W. P.; Zhang, B.; Cao, S.; Ren, Q. Y.; Shan, J. Q.** 2025. Numerical study of hydrodynamic melt jet fragmentation in sodium-cooled fast reactors based on the improved MPS method, Journal of Nuclear Science and Technology 62(10): 915-926. https://doi.org/10.1080/00223131.2025.2501300.
5. **Huang, C.; Liu, J.; Hai, L.; Dong, Z.; Niu, X**. 2022. Symmetric Heat Transfer Pattern of Fuel Assembly Subchannels in a Sodium-Cooled Fast Reactor, Symmetry 14(11): 2423. https://doi.org/10.3390/sym14112423
6. **Cangioli, F.; Chatterton, S.; Pennacchi, P.; Nettis, L.; Ciuchicchi, L.** 2018. Thermo-elasto bulk-flow model for labyrinth seals in steam turbines, Tribology International 119: 359-371. https://doi.org/10.1016/j.triboint.2017.11.016.
7. **Qin, H. Q.; Lu, D. G.; Zhong, D. W.; Wang, Y.; Song, Y.** 2020. Experimental and numerical investigation for the geometrical parameters effect on the labyrinth-seal flow characteristics of fast reactor fuel assembly, Annals of Nuclear Energy 135: 106964. https://doi.org/10.1016/j.anucene.2019.106964.
8. **Zhong, C.; Zhai, L.; Guo, J.; Cui, B.; Chen, G**. 2021.

Static Characteristics and Leakage Rates of Smooth Annular Seals Based on a New Solution Method for Gas-Liquid Two-Phase Conditions, Journal of Marine Science and Engineering 9(5): 523. https://doi.org/10.3390/JMSE9050523.

9. **Levanov, A. V.; Lapina, A. V.; Isaikina, O. Y**. 2024. Method for Determining the Ozone Mass Transfer Coefficient between the Gas and Liquid Phases in a Bubble Column Reactor, Russian Journal of Physical Chemistry A 98(7): 1461-1465 https://doi.org/10.1134/S0036024424700456.
10. **He, W. D.; Wang, C.; Zhang, Y. H.** 2015. Study of the influence of labyrinth seal clearance on gearbox leakage with gas-fluid two-phase mixture, Applied Mechanics and Materials 4113(789-790): 231-235. https://doi.org/10.4028/www.scientific.net/AMM.789-790.231
11. **Fu, Q.; Zhang, F.; Zhu, R. S.; Wang, X. L.** 2016. Effect of gas quantity on two-phase flow characteristics of a mixed-flow pump, Advances in Mechanical Engineering 8(4): 1-11. https://doi.org/10.1177/1687814016644578.
12. **Lu, X. L.; Andrés, L. S.; Yang, J.** 2022. A Nonhomogeneous Bulk Flow Model for Gas in Liquid Flow Annular Seals: An Effort to Produce Engineering Results, ASME Journal of Tribology 144(6): 062302. https://doi.org/10.1115/1.4052678.
13. **Zhai, L. L.; Chi, Z. H.; Guo, J.; Zhang, Z. J.; Zhu, Z. C.** 2018. Theoretical Solutions for Dynamic Characteristics of Liquid Annular Seals with Herringbone Grooves on the Stator Based on Bulk-Flow Theory, Science and Technology of Nuclear Installations 2018: 412154 https://doi.org/10.1155/2018/9412154
14. **Chen, P.; Wang, T.; Ma,W.; Xie, Z.; Yu, G.** 2022. CFD-Predicted Rotordynamic Characteristics for High-Temperature Water Liquid Seal Considering Tooth Deformation, Lubricants 10(10): 240. https://doi.org/10.3390/lubricants10100240.
15. **Wang, T.; Chen, P. W.; Ma, W. S.; Yu, G. B.** 2022. CFD-predicted on rotordynamic characteristics for high temperature sodium liquid seal, Journal of Theoretical and Applied Mechanics 60(3): 347-360. https://doi.org/10.15632/jtam-pl/150588.

B. Zhang, Q. Ma, P. Chen, Q. Duan, W. Ma, S. Li, G. Yu

CFD-PREDICTED ROTORDYNAMIC CHARACTERISTICS FOR LABYRINTH SEAL UNDER GAS-LIQUID TWO-PHASE CONDITIONS

S u m m a r y

In this study, computational fluid dynamics (CFD) was integrated with dynamic mesh technology and user-defined functions (UDFs), and the whirling motion equation was derived in detail. A numerical simulation investigation was conducted on the rotordynamic characteristics of labyrinth seals under gas-liquid two-phase conditions. The reliability of the numerical model was verified by experimental measurements of leakage flow rate, and the results showed that the variation trends of the two were consistent with a maximum relative error of 22.3%, indicating a good applicability of the model. The effects of three pressure drops, three rotor speeds and three different gas volume fractions (GVF) on the frequency-independent and frequency-dependent rotordynamic coefficients (including direct stiffness, cross-coupling stiffness, damping coefficients and effective coefficients) were analyzed systematically. The results demonstrated that an increase in pressure drop enhanced the direct stiffness and direct damping, while a rise in GVF led to a reduction in these coefficients; an increase in rotor speed improved the direct stiffness but decreased the direct damping, and exacerbated the negative effect of cross-coupling damping. The effective stiffness (K_{eff}) exhibited a parabolic variation trend with the whirling frequency, whereas the effective damping (C_{eff}) remained positive over the entire frequency range, which ensures the operational stability. This study provides a theoretical basis for the design and optimization of labyrinth seals in two-phase flow environments, and is conducive to improving the operational stability of industrial rotor systems.

Keywords: labyrinth seal, gas-liquid two-phase flow, rotordynamic characteristics, leakage flow, test rig.

Received January 28, 2026
Accepted June 19, 2026